

# Comparisons of bidirectional reflectance distribution function measurements on prepared particulate surfaces and radiative-transfer models

Hao Zhang and Kenneth J. Voss

To understand the connection between single-particle optics and the optics of a closely packed surface, controlled laboratory measurements of bidirectional reflectance distribution functions on layers of polymer and glass spheres are carried out. The measurements are compared with predictions from five radiative-transfer models; the Hapke's models, the Lumme-Bowell model, the BRDF algorithm of Mishchenko *et al.*, and the discrete ordinate radiative transfer. It is found that models of strict numerical radiative-transfer equations (RTEs) predict measurements well in some regions but have errors in both forward- and backward-scattering directions. The improved Hapke's model, although it has an anisotropic multiple-scattering term, still produces considerable errors compared with the strict RTE. The difference can be attributed to the exclusion of a diffraction contribution in the Hapke model. © 2005 Optical Society of America

OCIS codes: 010.4450, 280.0280, 290.5850, 290.4210, 030.5620, 300.0300.

## 1. Introduction

The relationship between the surface bidirectional reflectance distribution function (BRDF) of closely packed grain layers and the optical properties of the individual particles is an important problem in many scientific and engineering disciplines. However, there are many unanswered questions in this problem. Specifically how well does the radiative-transfer equation (RTE) work for closely packed particles? Are any single-scattering features of individual grains retained when the grains are touching? What are the effects of surface roughness on BRDF measurements? Can intrinsically forward-scattering particles have a back-scattering BRDF when aggregated?<sup>1-5</sup> Can diffraction be ignored when the filling factors of grain layers have high values?<sup>2,4,5</sup> How do analytical reflectance models such as Hapke's isotropic multiple-scattering approximation (HIMSA),<sup>6,7</sup> Hapke's anisotropic multiple-scattering approximation (HAMSA),<sup>8</sup> and the Lumme-Bowell (LB) model<sup>9</sup> work compared with strict RTE solutions such as the discrete ordinate ra-

diative transfer<sup>10</sup> (DISORT) program and Mishchenko *et al.*'s bidirectional reflection function (MBRF) algorithm?<sup>11</sup> Answers to these questions are also important in the remote sensing of planetary surfaces<sup>12-14</sup> and snow.<sup>15</sup>

In this study we perform controlled laboratory BRDF measurements of the powdered surfaces of 200- $\mu\text{m}$ -diameter polymer and 600- $\mu\text{m}$ -diameter glass spheres together with RTE calculations. For these nearly monodisperse spheres, with known particle-size distributions and real refractive indices, we determine first the single-scattering quantities of the particles including the phase function, single-scattering albedo, asymmetry parameter, and scattering and extinction efficiencies by using Mie theory.<sup>16,17</sup> Then we introduce these single-scattering quantities into the RTE models and compare them with the measurements.

## 2. Brief Outline of the Models

The models mentioned in Section 1 are chosen for this study because they are representative and used extensively in remote-sensing applications. Strict numerical RTE solutions such as DISORT and the MBRF are widely used as benchmarks in testing semiempirical models.<sup>8,18</sup> On the other hand, Hapke's models and the LB model are approximate solutions of the RTE but have closed-form expressions that contain some physical quantities explicitly. We

The authors are with the Department of Physics, University of Miami, P.O. Box 248046, Coral Gables, Florida 33124-8046. K. Voss' e-mail address is voss@physics.miami.edu.

Received 12 July 2004; accepted 13 August 2004.

0003-6935/05/040597-14\$15.00/0

© 2005 Optical Society of America

present the models in the form of the reflectance factor<sup>7</sup> (REFF) in order to compare them with measurements directly. To be self-contained, unified symbols are used in all models instead of their original notation. The symbols are introduced in the order of their appearances in the models.

The bidirectional reflectance  $r$ , BRDF, and REFF are defined, respectively, as<sup>7</sup>

$$r = \frac{dL_R}{dE_i}, \quad (1)$$

$$\text{BRDF} = \frac{r}{\cos \theta_i}, \quad (2)$$

$$\text{REFF} = \pi \text{BRDF} = \frac{\pi r}{\cos \theta_i}, \quad (3)$$

where  $dL_R$  is the reflected radiance,  $dE_i$  is the incident collimated irradiance, and  $\theta_i$  is the incident zenith angle. The REFF is convenient because it gives a direct comparison of the reflectance of a surface with that of a perfect Lambertian surface.

#### A. HIMSA Model

The HIMSA model<sup>7</sup> solves the single scattering exactly and approximates the multiple scattering as isotropic:

$$\begin{aligned} \text{REFF}_{\text{HIMSA}}(\mu_0, \mu, \alpha) = & \frac{\varpi_0}{4} \frac{1}{\mu_0 + \mu} \{ [1 + B(\alpha)] P(\alpha) \\ & + H(\mu) H(\mu_0) - 1 \} \\ & \times S(\mu_0, \mu, \phi, \bar{\theta}), \end{aligned} \quad (4)$$

where  $\mu_0$ ,  $\mu$ ,  $\phi$ , and  $\alpha$  are the cosine of the incident zenith, the cosine of the viewing zenith, the relative azimuth angle, and the phase angle, respectively.  $P(\alpha)$  is the single-scattering phase function that is normalized to  $4\pi$  throughout this work,  $\varpi_0$  is the single-scattering albedo, and  $H(x)$  is Chandrasekar's  $H$  function<sup>19</sup> approximated by<sup>8</sup>

$$H(x) \approx \frac{1}{1 - \varpi_0 x \left( r_0 + \frac{1 - 2r_0 x}{2} \ln \frac{1 + x}{x} \right)}, \quad (5)$$

where

$$r_0 = \frac{1 - (1 - \varpi_0)^{1/2}}{1 + (1 - \varpi_0)^{1/2}}. \quad (6)$$

$B(\alpha)$  is the enhanced backscattering (hot-spot) correction factor:

$$B(\alpha) = \frac{B_0}{1 + \frac{1}{h} \tan \frac{\alpha}{2}}, \quad (7)$$

where parameters  $B_0$  and  $h$  control the amplitude and angular width of the hot spot, respectively.  $S(\mu_0, \mu, \phi, \bar{\theta})$  is the surface-roughness correction factor;  $\bar{\theta}$  is the average topographic slope angle of the surface, and it alters the local incidence and emergence angles.

#### B. HAMS Model

In this version of the Hapke model the single-scattering part remains the same while the multiple-scattering part is replaced by a more anisotropic term. Since in this work our samples are very large spheres where coherent backscattering<sup>20,21</sup> is unlikely to be observable with the instrument (see Subsection 3.A), we adopt the HAMS model without the coherent backscattering correction term:

$$\begin{aligned} \text{REFF}_{\text{HAMS}}(\mu_0, \mu, \alpha) = & \frac{\varpi_0}{4} \frac{1}{\mu_0 + \mu} \\ & \times \{ [1 + B(\alpha)] P(\alpha) \\ & + M(\mu_0, \mu) \}, \end{aligned} \quad (8)$$

where

$$\begin{aligned} M(\mu_0, \mu) = & \Pi(\mu_0)[H(\mu) - 1] + \Pi(\mu)[H(\mu_0) - 1] \\ & + \Delta[H(\mu) - 1][H(\mu_0) - 1], \end{aligned} \quad (9)$$

$$\Pi(x) = 1 + \sum_{n=1}^{\infty} A_n b_n P_n(x), \quad (10)$$

$$\Delta = 1 + \sum_{n=1}^{\infty} A_n^2 b_n, \quad (11)$$

$$A_n = 0 \quad n \text{ even}, \quad (12)$$

$$A_n = \frac{(-1)^{\frac{n+1}{2}}}{n} \frac{1 \times 3 \times 5 \times \dots \times n}{2 \times 4 \times 6 \times \dots \times (n+1)} \quad n \text{ odd}, \quad (13)$$

and the terms  $b_n$  are the Legendre expansion coefficients of the phase function:

$$P(\alpha) = 1 + \sum_{n=1}^{\infty} b_n P_n(\cos \alpha). \quad (14)$$

#### C. Lumme-Bowell Model

The LB<sup>9,22-24</sup> model assumes that the single scattering by a layer of particles comes from three distinct parts: shadowing, roughness, and particle scattering. The multiple scattering part is approximated by the  $H$  function, as with Hapke's model, but with the scaled single-scattering albedo as an argument.<sup>23</sup> Note that the original LB model paper<sup>9</sup> does not have an explicit expression for a multiple-scattering term while that given in Ref. 23 has a typographic error with the  $1/(\mu + \mu_0)$  factor missing. Here we adopt the form as a combination of Refs. 22-24:

$$\begin{aligned} \text{REFF}_{\text{LB}}(\mu_0, \mu, \alpha) &= R_S + R_M = \frac{\varpi_0}{4} \frac{1}{\mu + \mu_0} \\ &\times [2\Phi_R \Phi_S P(\alpha) + H(\mu, \varpi_0^*) \\ &\times H(\mu_0, \varpi_0^*) - 1], \end{aligned} \quad (15)$$

where  $R_S$  is the single-scattering term,  $R_M$  is the multiple-scattering term, and  $\varpi_0^*$  is the scaled single-scattering albedo according to the similarity relations:

$$\varpi_0^* = \frac{1-g}{1-g\varpi_0} \varpi_0, \quad (16)$$

where  $g$  is the asymmetry parameter given by

$$g = \langle \cos \alpha \rangle = \frac{1}{2} \int_{-1}^1 P(\cos \alpha) d(\cos \alpha). \quad (17)$$

$\Phi_R$  is the surface-roughness correction factor given by

$$\Phi_R = \frac{1 + (1-q)\rho\xi}{1 + \rho\xi}, \quad (18)$$

where  $q$  is the fraction of the surface covered with holes and  $\rho$  is the mean slope of holes on a rough surface:

$$\rho = \frac{H}{R} = \tan(\bar{\theta}), \quad (19)$$

where  $H$  and  $R$  are the depth and the radius of a hole, respectively. The angular quantity  $\xi$  is given as

$$\xi = \frac{(\mu^2 + \mu_0^2 - 2\mu\mu_0 \cos \alpha)^{1/2}}{\mu\mu_0}. \quad (20)$$

The term  $\rho$  may be estimated for packed spheres with certain filling factors.<sup>9</sup>  $\Phi_S$  is the shadow hiding factor and for spherical particles is given by<sup>9,24</sup>

$$\Phi_S \approx \frac{y + 3/4}{y + 3/2}, \quad (21)$$

$$y = \frac{D}{2.38} \frac{\mu + \mu_0}{(\mu^2 + \mu_0^2 - 2\mu\mu_0 \cos \alpha)^{1/2}}, \quad (22)$$

where  $D$  is the volume density or the filling factor.

#### D. MBRF Model

The single-scattering phase function is expanded as a Fourier series<sup>11</sup>:

$$P(\mu, \mu_0, \phi) = P^0(\mu, \mu_0) + 2 \sum_{m=1}^{m_{\max}} P^m(\mu, \mu_0) \cos(m\phi), \quad (23)$$

where the Fourier components of the  $m$ th order are given by the expansion in terms of the generalized spherical functions  $P_{mn}^s$  as

$$P^m(\mu, \mu_0) = (-1)^m \sum_{s=m}^{s_{\max}} \beta_s P_{m0}^s(\mu) P_{m0}^s(\mu_0), \quad (24)$$

and  $\beta_s$  are coefficients in the Legendre polynomial expansion of the phase function:

$$P(\Theta) = \sum_{s=0}^{s_{\max}} \beta_s P_s(\cos \Theta), \quad (25)$$

where  $\Theta$  is the scattering angle,

$$\Theta = \pi - \alpha. \quad (26)$$

The intensity of the reflected radiation from a flat surface is defined as

$$L(-\mu, \phi) = \mu_0 R(\mu, \mu_0, \phi) F, \quad (27)$$

where  $\pi F$  is the collimated incident flux per unit area perpendicular to the incident beam and  $R(\mu, \mu_0, \phi)$  is the bidirectional reflection function.  $R(\mu, \mu_0, \phi)$  is expanded as a Fourier series in the azimuth angle:

$$R(\mu, \mu_0, \phi) = R^0(\mu, \mu_0) + 2 \sum_{m=1}^{m_{\max}} R^m(\mu, \mu_0) \cos m\phi, \quad (28)$$

where the coefficients  $R^m(\mu, \mu_0)$  are solved by Ambarsumian's nonlinear integral equation<sup>25</sup> once  $P^m(\mu, \mu')$  is known:

$$\begin{aligned} (\mu + \mu_0) R^m(\mu, \mu_0) &= \frac{\varpi_0}{4} P^m(-\mu, \mu_0) + \frac{\varpi_0}{2} \mu_0 \\ &\times \int_0^1 P^m(\mu, \mu') R^m(\mu', \mu_0) d\mu' \\ &+ \frac{\varpi_0}{2} \mu \int_0^1 R^m(\mu, \mu') P^m(\mu', \mu_0) d\mu' \\ &+ \varpi_0 \mu \mu_0 \int_0^1 \int_0^1 R^m(\mu, \mu') P^m(-\mu', \mu'') \\ &\times R^m(\mu'', \mu_0) d\mu' d\mu''. \end{aligned} \quad (29)$$

Thus the REFF for the MBRF is

$$\text{REFF}_{\text{MBRF}} = \pi \frac{L}{\pi F} = R. \quad (30)$$

#### E. DISORT

DISORT<sup>10,26</sup> belongs to the class of discrete-ordinate solutions to the RTE. Among these five models only DISORT allows layers with finite optical thickness

while all five allow semi-infinite layers. The RTE can be written as

$$\mu \frac{dL(\tau, \mu, \phi)}{d\tau} = L(\tau, \mu, \phi) - \frac{\varpi_0}{4\pi} \int_0^{2\pi} d\phi' \times \int_{-1}^1 d\mu' P(\mu, \phi; \mu', \phi') L(\tau, \mu', \phi'), \quad (31)$$

where  $\tau$  is the optical thickness. By expanding the radiance  $L$  in terms of the Fourier series, we obtain

$$L(\tau, \mu, \phi) = \sum_{m=0}^{2M-1} L^m(\tau, \mu) \cos m\phi, \quad (32)$$

and the single-scattering phase function  $P$  in a series of Legendre polynomials,

$$P(\mu, \phi; \mu', \phi') \equiv P(\cos \Theta) = \sum_{l=0}^{2M-1} (2l+1) g_l P_l(\cos \Theta), \quad (33)$$

and by taking advantage of the addition theorem for spherical harmonics,<sup>19,26</sup> we obtain

$$P(\cos \Theta) = \sum_{l=0}^{2M-1} (2l+1) g_l \left[ P_l(\mu) P_l(\mu') + 2 \sum_{m=1}^l \Lambda_l^m(\mu) \Lambda_l^m(\mu') \cos m(\phi - \phi') \right], \quad (34)$$

where

$$\Lambda_l^m(\mu) = \left[ \frac{(l-m)!}{(l+m)!} \right]^{1/2} P_l^m(\mu) \quad (35)$$

is the normalized associated Legendre polynomial of the ordinary associated Legendre polynomial  $P_l^m(\mu)$ . The RTE is split into  $2M$  independent integrodifferential equations

$$\mu \frac{dL^m(\tau, \mu)}{d\tau} = L^m(\tau, \mu) - \frac{\varpi_0}{2} \int_{-1}^1 \left[ \sum_{l=0}^{2M-1} (2l+1) g_l \Lambda_l^m(\mu) \Lambda_l^m(\mu') \right] \times L^m(\tau, \mu') d\mu'. \quad (36)$$

When the integral is approximated by a Gaussian quadrature sum, the above integrodifferential equation

is transformed into a system of ordinary differential equations,

$$\mu_i \frac{dL^m(\tau, \mu_i)}{d\tau} = L^m(\tau, \mu_i) - \sum_{\substack{j=-N \\ j \neq 0}}^N w_j D^m(\tau, \mu_i, \mu_j) L^m(\tau, \mu_j) \times (\iota = \pm 1, \pm 2 \dots \pm N), \quad (37)$$

and solved with appropriate boundary conditions. When the incident collimated flux is specified to be  $\pi / \mu_0$ , the REFF for DISORT is then

$$\text{REFF}_{\text{DISORT}} = L_{\text{DISORT}}, \quad (38)$$

where  $L_{\text{DISORT}}$  is the DISORT code's output radiances.

#### F. Remarks on the Models

Despite their very different approaches to modeling the radiative transfer in packed surfaces, the HIMSA and the LB model have an identical form for a smooth (zero surface roughness and no hot-spot) surface:

$$\text{REFF}_{\text{Smooth}}(\mu_0, \mu, \alpha) = \frac{\varpi_0}{4} \frac{1}{\mu_0 + \mu} [P(\alpha) + HH - 1], \quad (39)$$

which is obtained by letting the filling factor (or volume density and surface density in the LB model) approach zero and therefore

$$B(\alpha) \rightarrow 0, \quad \Phi_R \rightarrow 1, \quad \Phi_S \rightarrow 1/2. \quad (40)$$

Equation (39) is further reduced to the classical RTE solution for a sparse semi-infinite medium (single-scattering) approximation by letting  $H$  approach 1,

$$\text{REFF}_{\text{Single}} = \frac{\varpi_0}{4} \frac{1}{\mu + \mu_0} P(\alpha). \quad (41)$$

For isotropic scatters with  $P(\alpha) = 1$ , Eq. (41) gives the Lommel–Seeliger law. For layers with finite optical thickness  $\tau$ , the REFF in the single-scattering approximation may be given by<sup>25,27</sup>

$$\text{REFF}_{\text{Single}} = \frac{\varpi_0}{4} \frac{1}{\mu + \mu_0} P(\alpha) \times \left\{ 1 - \exp \left[ -\tau \left( \frac{1}{\mu} + \frac{1}{\mu_0} \right) \right] \right\}. \quad (42)$$

The Hapke surface-roughness correction applies to both single and multiple scattering. The LB roughness factor is applied only to the single-scattering term, thus was criticized by Hapke.<sup>28,29</sup> If the LB model's roughness factor is applied to entire RTE models, the reciprocity relation still holds; hence the relation is physically plausible.

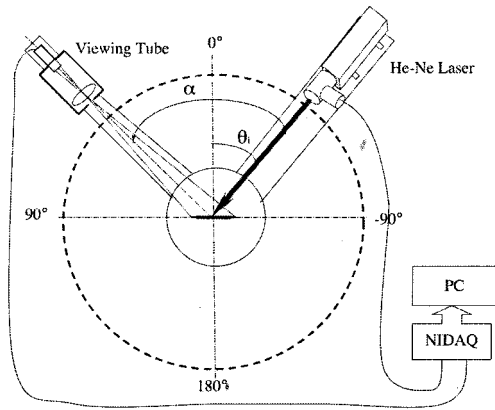


Fig. 1. Schematic of the simple goniometric scattering meter setup. Throughout this study the incident zenith angle  $\theta_i$  is specified to be negative. Phase angle  $\alpha$  is specified to be positive when opposite the incident beam.

Both the HIMSA and the LB models assume that, for closely packed particulate media, the phase function does not include the diffraction peak. This is equivalent to treating the forward scattering as indistinguishable from the transmitted radiation. Thus in principle when the Mie phase function is introduced into these two models, the diffraction peak should be removed. However, this is not necessary since the reflectance region does not include direct forward scattering and the isotropic multiple-scattering terms in these two models do not contain any quantities that are derived from the phase function. In the HANSA model<sup>8</sup> it is not clearly stated whether the diffraction peak should be removed from Eqs. (8)–(14).

Mishchenko<sup>2</sup> verified, by performing the Percus–Yevick structural factor calculations,<sup>2,30,31</sup> that this assumption holds when the filling factor  $f$  roughly exceeds 0.2. He found that the effect of packing is especially significant at  $\Theta \leq 0.4\lambda/r_0$ , where  $\lambda$  and  $r_0$  are the wavelength and the particle radius, respectively. Mishchenko and Macke<sup>4</sup> also emphasized, however, that there is no critical value of  $f$  before which the diffraction contribution is 50% ( $f = 0$ ) and after which it is 0 ( $f = 1$ ). In the current study the closely packed spheres have filling factors greater than 0.5; however,  $0.4\lambda/r_0$  is only  $\sim 0.1^\circ$ . Thus the full Mie phase functions are to be supplied to all five models, and the diffraction effects are discussed in Section 5.

### 3. Instruments, Samples, and Measurement Descriptions

#### A. Simple Goniometric Scattering Meter

To perform scattering measurements on the prepared surfaces of packed spheres, a simple goniometric scattering meter was built, as shown in Fig. 1. A Melles–Griot unpolarized He–Ne laser (632.8-nm wavelength) serves as the light source. After being expanded by a beam expander, the light is polarized

by a linear polarizer. Next the linearly polarized beam is split into two orthogonal polarized beams by a CVI polarizing beam-splitting cube: One beam goes to a monitor photodiode and the other to the sample. By rotating the polarizing cube, incident beams with polarizations both parallel  $p$  and perpendicular  $s$  to the scattering plane can be achieved. The viewing tube consists of a narrowband interference filter, a focusing lens, and a photodiode with electronics. In this configuration the full angular resolution is  $2.9^\circ$ , which is determined by the ratio of the aperture diameter (1.57 cm) to the radial distance of the aperture to the sample plane (31 cm). With a converging lens ( $f = 2.77$  mm) behind the interference filter the sampled area is a circle with a diameter of 36 mm.

The alignment of the goniometer including the sample holder orientation and the incident and viewing directions is checked by a digital protractor. The angular error is estimated to be less than  $1.5^\circ$ . The measured REFF on a Labsphere nominal 99% reflectance plaque agrees with previous measurements<sup>32</sup> within 2% less than the  $70^\circ$  viewing angle and within  $\sim 4\%$  greater than the  $70^\circ$  viewing angle.

Before and after each measurement sequence a laser-power stability test is performed. Although the laser-power fluctuations could be eliminated by taking a ratio of the sample and the monitor channel, it has been found that when the warmup time is sufficient the He–Ne laser fluctuations in the viewing channel can be within 1%, and using the monitor channel adds unnecessary noise. Before and after the measurement dark signals are recorded, and their average is subtracted from the measurement.

Sample holders include two polyvinyl chloride holders with depths of 10 and 15 mm. To minimize any bottom reflectance, black construction paper is placed in the bottom of the sample holder during the measurements.

At normal illumination the circular illuminated spot on a flat sample is 13 mm in diameter, and at  $60^\circ$  incidence the spot is elongated to  $26 \times 13$  mm. Numerical calculations<sup>33</sup> show that when the beam radius is  $\sim 10$  times larger than the sphere radius, the incident beam can be regarded as an infinite plane wave. Since our largest sample are glass spheres with a nominal diameter of 0.6 mm, this condition is comfortably satisfied.

#### B. Samples, Measurements, and Calibrations

##### 1. Samples

Two different types of spherical particle are employed in this study: polystyrene spheres with a nominal diameter of 200  $\mu\text{m}$  from Duke Scientific Corporation (catalog number 4320) and silicon glass spheres with a nominal diameter of 600  $\mu\text{m}$  from Whitehouse Scientific (catalog number MS0589). Major reasons for choosing these spheres are the following: (1) Both are commercially available and National Institute of Science and Technology (NIST) traceable. (2) These particle sizes are commensurate with the size of natural sediment.<sup>34,35</sup> (3) The Mie phase functions (see Sec-

tion 4) of both kinds of sphere have steep drop-off features around the rainbow region. Such characteristics may be used as indications of the single-scattering features in reflectance measurements of aggregated spheres.

### 2. Measurement Descriptions

The current goniometer's configurations allow the incident light to be either *p*- or *s*-polarized while only the unpolarized scattered radiance is collected. For comparison with the RTE models mentioned above, we take the average of these two incident polarizations to get the unpolarized case. The spheres are slowly poured into the sample holder to make a layer of spheres, and the sample holder mount is slightly rocked to settle the grains. Next the edge of a ruler is moved in different directions on the surface of the holder to make the surface macroscopically flat. Each sample layer is made at least twice to obtain the sample-to-sample variations caused by different surfaces.

To test for laser-interference problems, we mapped the backscattering pattern of a single layer of the 200- $\mu\text{m}$  spheres by setting a white screen behind the laser and illuminating the sample at normal incidence. As many as 10 rings, including the primary, the secondary rainbows, and eight supernumerary bows could be identified. The angular positions of these rings showed good agreement with Mie calculations; thus no coherence problems should exist.

### 3. Calibrations

For reflectance data the radiance of the sample is ratioed to that of a Labsphere calibration plaque with a nominal 99% reflectance to get the REFF according to Eq. (3). However, in reality the reflectance of a plaque can never be perfectly Lambertian; thus a correction is applied to the REFF as follows<sup>36</sup>:

The raw REFF may be expressed as

$$\text{REFF}^{\text{raw}} = \frac{1}{2} \left( \frac{L_l^s}{L_c^s} + \frac{L_l^p}{L_c^p} \right), \quad (43)$$

where  $L$  is the recorded radiance; *s* and *p* are *s*- and *p*-polarizations, respectively; *l* and *c* are the sample and the calibration plaque, respectively. The correction factor is introduced as

$$\text{Corr} = \frac{1}{2} \frac{(L_c^s + L_c^p)}{\cos(\theta_v)} f(\theta_v^0), \quad (44)$$

where  $\theta_v$  is the viewing zenith angle and  $f(\theta_v^0)$  is a constant. The first part of this factor is the radiance reflected off the calibration plaque divided by the cosine of the viewing angle. Ideally this should be a flat line, but we have found that this curve falls  $\sim 15\%$  at higher viewing angles. The second part  $f(\theta_v^0)$  is a scaling factor that brings the REFF at a specific viewing zenith angle to that of the value of Ref. 32. For

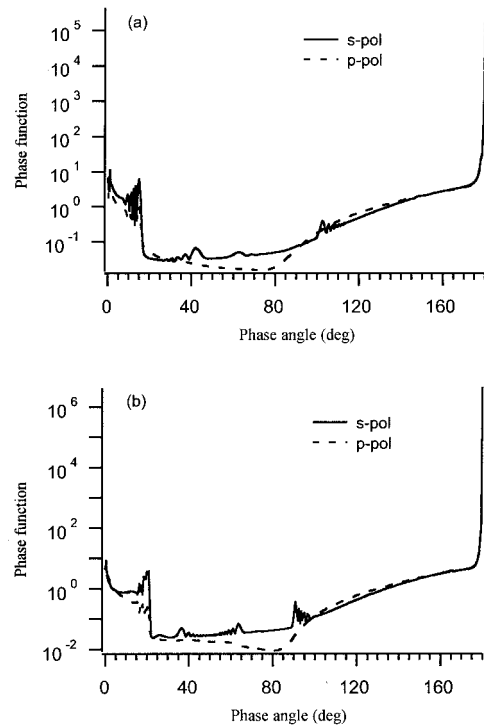


Fig. 2. Mie phase functions of (a) 200- and (b) 600- $\mu\text{m}$  spheres: *s*-pol, *p*-pol, electric field of the incident irradiance perpendicular and parallel to the scattering plane, respectively. The unpolarized Mie phase function is their average.

example, at normal incidence the REFF at the 45° viewing zenith is 0.99, and at 60° incidence the REFF at the 0° viewing zenith is 0.972. The final form of the REFF is then

$$\text{REFF}^{\text{Gonio}} = \text{REFF}^{\text{raw}} \times \text{Corr}. \quad (45)$$

## 4. Modeling Results and Comparisons with Measurements

### A. Mie Results of the Spheres

Mie calculations were done with both Mishchenko *et al.*'s algorithm<sup>11,37,38</sup> and the MieV code,<sup>39,40</sup> and the results agreed very well. To be consistent within this study, all Mie-derived quantities to supply the RTE models were calculated by the former.

The 200- $\mu\text{m}$  (Duke4320) spheres have a very narrow Gaussian size distribution:

$$f(D) = \frac{1}{(2\pi)^{1/2}\sigma} \exp\left[-\frac{(D - D_0)^2}{2\sigma^2}\right], \quad (46)$$

where  $D_0 = 197 \mu\text{m}$  and  $\sigma = 6.1 \mu\text{m}$  (provided by Duke Scientific). With a refractive index of 1.59 at a 632.8-nm wavelength, Mie phase functions for both *p* and *s* polarizations are shown in Fig. 2(a). The size

distribution of the 600- $\mu\text{m}$  sample (WH0589) is fit to a lognormal distribution<sup>38,41</sup>:

$$f(D) = \frac{1}{w_0 D} \exp \left[ -\frac{\left( \ln \frac{D}{D_0} \right)^2}{2(\ln \sigma)^2} \right], \quad (47)$$

where  $w_0 = 0.0216$ ,  $D_0 = 587.6 \mu\text{m}$ , and  $\sigma = 1.0186$ . The Mie phase functions shown in Fig. 2(b) are calculated with a refractive index of 1.52 for silicon glass.

As a first-order approximation the imaginary refractive indices for both types of spheres are assumed to be 0. This is discussed below.

### B. Estimations of the Optical Thickness

In RTE calculations the optical thickness  $\tau$  is more frequently used than geometric depth  $z$ . It is also one of the inputs of DISORT. The definition of  $\tau$  may be written as<sup>7,42</sup>

$$\tau = N\sigma_{\text{ext}}z, \quad (48)$$

where  $N$  is the number of identical particles per unit volume,  $\sigma_{\text{ext}}$  is the extinction cross section, and  $z$  is the geometrical depth. For a distribution of particles

$$\tau = \int_0^s N(z)\langle\sigma_{\text{ext}}(z)\rangle dz \approx \langle N \rangle \langle \sigma_{\text{ext}} \rangle s, \quad (49)$$

where

$$\langle N \rangle = \frac{n}{\bar{V}} = \frac{f}{\frac{4}{3} \pi r_{\text{eff}}^3} \quad (50)$$

is the size-averaged number density,  $r_{\text{eff}}$  is the size-averaged radius, and  $f$  is the filling factor. For the large spheres used in this study  $\langle\sigma_{\text{ext}}\rangle$  is essentially  $2\pi r_{\text{eff}}^2$ ; thus the optical thickness is roughly<sup>43</sup>

$$\tau \approx \frac{3fs}{2r_{\text{eff}}}, \quad (51)$$

where  $s$  is the layer's geometric thickness. The filling factors for both samples have been evaluated by estimating the number of spheres in the sample holders and the volumes that they occupy.

The models, other than DISORT, calculate only reflectance from semi-infinite layers; thus  $\tau$ , which can be considered optically thick for each sample, is needed. Bohren<sup>42</sup> has shown that a layer can be taken as optically thick when

$$\tau \geq \frac{200}{1-g} = \tau_{\infty}. \quad (52)$$

Table 1. Parameters Used in the Modeling

Samples	$f$	$s$	$\tau$	$\tau_{\infty}$	$g$	$\varpi_0$	$N$	$NK$	NSTR
Duke4320	0.60	10	88.5	1000	0.8	0.999	100	100	100
WH0589	0.54	15	41.25	1111	0.82	0.99	100	100	100

Note:  $f$ , filling factor (or  $D$ , the volume density in the LB model);  $s$ , geometrical depth of the layer (in millimeters);  $\tau$ , optical thickness;  $\tau_{\infty}$ , asymptotic value given by Eq. (52);  $g$ , asymmetry parameter;  $\varpi_0$ , single-scattering albedo;  $N$ ,  $NK$ , number of intervals in the size distribution sum and the number of quadrature angles within each  $N$ , respectively, in MBRF's Mie algorithm; NSTR, number of computational angles (number of streams) used in DISORT. The other parameters are introduced in the text.

Layers satisfying this criterion have reflectance within 1% of its asymptotic value. The optical thicknesses are listed in Table 1 along with other RTE model input quantities for each sample. It is obvious that both samples used in this study are much thinner than the criterion of the semi-infinite. This issue is also discussed in Subsection 4.D.

### C. Estimations of the Filling Factors

Filling factors for the 200- and 600- $\mu\text{m}$  spheres are evaluated by estimating the number of spheres in the sample holders and the volume of the holders. For the 200- $\mu\text{m}$  spheres, the number is estimated to be around 0.6, a typical value of the random close packing of monodisperse spheres.<sup>44</sup> For the 600- $\mu\text{m}$  spheres, however, the result is 0.54. This smaller value may be attributed to the larger spheres not being packed as efficiently because of the larger dispersion in size, imperfections in shape, or the finite size of the holder. This filling factor is still greater than the lower limit that occurs with layers of spheres stacked one on top of the other ( $f = 0.524$ ).

### D. Effects of Absorbing Spheres and Finite Optical Thickness

Unfortunately, accurate values of the imaginary refractive indices  $n_i$  of the spheres used in this study are unavailable from their manufacturers; hence the Mie functions are calculated first by assuming that  $n_i = 0$ ; thus  $\varpi_0 = 1$ . However, any  $\varpi_0$  values supplied to the RTE models should be less than 1 to be physically correct,<sup>4</sup> and this value is crucial to the RTE results for strong multiple-scattering media. For example, the diffuse reflectance values calculated by DISORT varying by only  $\varpi_0 = 0.999$  ( $n_i \approx 10^{-6}$ ) and  $\varpi_0 = 0.9999$  ( $n_i \approx 10^{-7}$ ) differ by as much as 10% at normal incidence for the 200- $\mu\text{m}$  spheres. In contrast the Mie phase functions and the asymmetry parameter change by less than 0.6% and 0.1% ( $g = 0.8028$  for  $n_i = 0$  to  $g = 0.8033$  for  $n_i = 10^{-6}$ ), respectively, in going from  $n_i = 0$  to  $n_i = 10^{-6}$ . Since the  $n_i = 10^{-6}$  value leads to an absorption coefficient<sup>17</sup> of  $a = [(4\pi n_i) / \lambda] \approx 20/m$  and both types of sphere used in this study are large clear spheres, the actual  $n_i$  values for these spheres are unlikely to be much higher than the order of  $10^{-6}$ .

The single-scattering parameters that supply the models are chosen in the following way. First, we verify that the Mie phase functions for a single size [mean size  $D_0$  in Eqs. (46) and (47)] and for the size-averaged case are the same in the sense of the overall trend and the baseline level. This is also true in the resultant REFF, as predicted by any of the five RTE models when the phase functions are inserted. Then we run DISORT with the appropriate optical thickness (88.5 for the 200- $\mu\text{m}$  spheres or 41.25 for the 600- $\mu\text{m}$  spheres) supplied with Mie quantities calculated with varying  $n_i$  values from 0,  $10^{-8}$ ,  $10^{-7}$  to as great as  $10^{-3}$  where the rainbow structures totally disappear. These calculations are compared with the measurements. The results indicate that the appropriate  $n_i$  for 200- $\mu\text{m}$  spheres is between  $10^{-7}$  and  $10^{-6}$ ; hence the single-scattering albedo is  $\sim 0.999$ . This  $\varpi_0$  and the  $n_i = 0$  phase function is chosen for the 200- $\mu\text{m}$  spheres. For the 600- $\mu\text{m}$  spheres  $n_i$  is between  $10^{-6}$  ( $\varpi_0 = 0.995$ ) and  $10^{-5}$  ( $\varpi_0 = 0.95$ ). The  $n_i = 5 \times 10^{-6}$  ( $\varpi_0 \approx 0.97$ ) value roughly corresponds to an absorption coefficient of 100 /m, which seems too high from the discussions above. Thus for 600- $\mu\text{m}$  spheres we still use the phase function with  $n_i = 0$  but  $\varpi_0 = 0.99$  to account for the absorption effects. This choice for the 600- $\mu\text{m}$  spheres is heuristic, thus less accurate than for the 200- $\mu\text{m}$  spheres.

Recent measurements of the complex refractive index on polystyrene microspheres<sup>45</sup> give  $n_i \approx 4 \times 10^{-4}$  (corresponding to an absorption coefficient of 8000 /m) at visible wavelengths. When this value is supplied to the Mie and RTE models, the rainbow features in the resultant REFF are very small in contrast to the strong features in the measurements, and the predicted REFF values are much lower than the measurements.

As mentioned above, our sample thicknesses were not sufficient to meet the Bohren criterion<sup>42</sup> as being in the asymptotic region. However, calculations with DISORT show that with  $\varpi_0 = 0.999$  the REFF of a  $\tau = 1000$ , 200- $\mu\text{m}$ -sphere layer is typically within 0.5% of a  $\tau = 88.5$  layer for all phase angles at the three illumination angles, and with  $\varpi_0 = 0.99$  the REFF of a  $\tau = 1111$ , 600- $\mu\text{m}$ -sphere layer is typically less than 0.2% higher than  $\tau = 41.25$  over all phase angles at both normal and 60° illuminations. Thus our BRDF measurements can be compared with reflectance models for semi-infinite layers.

### E. Data

Figure 3 shows the raw REFF [Eq. (43)] of a 10-mm-thick layer of the 200- $\mu\text{m}$  spheres with  $p$ - ( $p$ -pol) and  $s$ -polarized ( $s$ -pol) incidence at 60° zenith. When compared with the Mie counterparts shown in Fig. 2(a), one can see that the reflectance curves for the two orthogonal polarizations resemble their respective Mie phase functions. Besides the strong rainbow peak that appears in the  $s$ -pol, the second rainbow peak<sup>46</sup> around the 100° phase angle (or 40° viewing angle in this configuration) is also present. The peaks above the 130° phase (70° viewing angle),

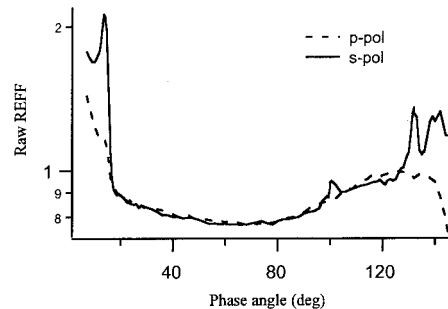


Fig. 3. Raw REFF of a 10-mm-thick, 200- $\mu\text{m}$ -sphere layer for two orthogonal incident polarizations at  $-60^\circ$  incidence. The viewing zenith angle in this configuration is a phase angle minus  $60^\circ$ .

however, must be caused by surface roughness since they do not repeat consistently in repeated measurements with different surface realizations. The  $p$ -pol, on the other hand, exhibits only a shoulder around the rainbow region and remains featureless throughout the rest of the region, closely resembling its  $p$ -polarization phase function. It is also seen that the steep drop-off features on the larger phase angle side of the rainbow present in the Mie phase functions for both polarizations are preserved in the respective REFF. However, many of the Mie features present in  $s$ -polarizations such as the peaks around the 40° phase angle disappear in the  $s$ -pol. As we show in Section 5, these peaks are washed out by strong multiple scattering in the diffuse reflection region.

Both DISORT and MBRF are strict solutions of the RTE and may give similar predictions, so we present first a comparison study of the two. Note that both the MBRF and DISORT converge well before the number of quadrature angles used in the angular integrations for solving the RTE (the variable NG in the MBRF code and NSTR in DISORT) reaches 200 for the 200- $\mu\text{m}$  spheres with  $\varpi_0 = 0.999$  described above. Since the MBRF is for semi-infinite layers only,  $\tau = 2000$  is supplied to DISORT (although  $\tau = 1000$  already appears to be the asymptotic value). In Fig. 4 the predictions are plotted for the 200- $\mu\text{m}$  spheres by the two models supplied with the same Mie input at an angular resolution of  $0.5^\circ$  with an NG of 200 for MBRF and NSTR of 200 for DISORT. It is seen from these data that the two models agree with each other very well in the diffuse reflectance region but differ in the phase angle range between  $10^\circ$  and  $15^\circ$ . The difference grows with the incident zenith angle. The maximum difference is 3% (normal incidence), 5.6% ( $35^\circ$ ), and 17% ( $60^\circ$ ). In this rainbow region MBRF has fewer oscillations than DISORT. Since the optical thickness can be varied in DISORT and most of the sample layers used in this study have finite thickness, we use DISORT to represent the strict RTE solution but keep in mind that it could be off by several percentage points at the rainbow peaks. Also, to compare the models, we neglect first the

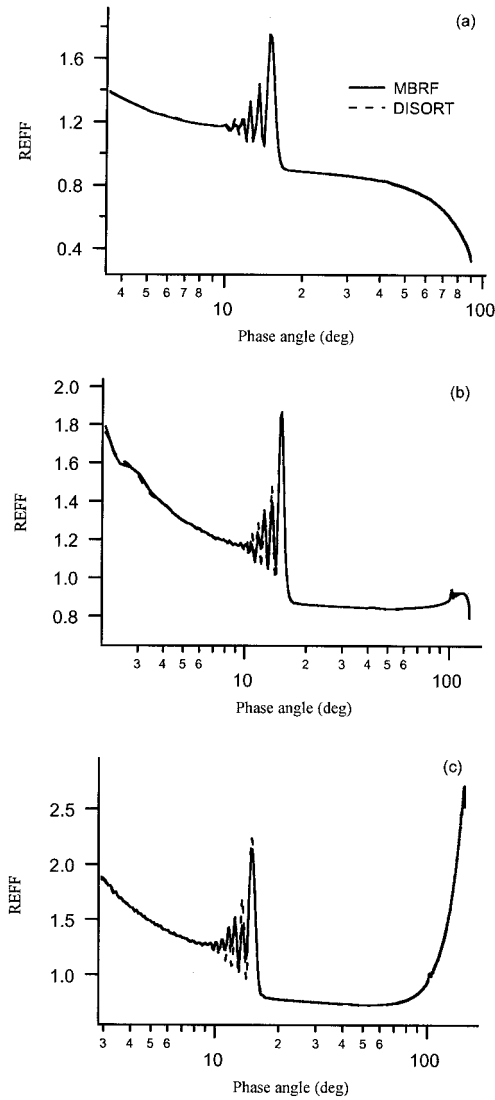


Fig. 4. Comparisons of MBRF and DISORT for a 200- $\mu\text{m}$ -sphere layer with  $\tau = 2000$  and  $\varpi_0 = 0.999$ . Incident zenith angles are (a)  $0^\circ$ , (b)  $-35^\circ$ , and (c)  $-60^\circ$ .

backscattering (or shadowing) factors and the surface roughness factors in the Hapke and LB models.

Figure 5 shows a comparison of the models with the goniometer reflectance data for the 200- $\mu\text{m}$ -sphere sample at three illumination angles. It can be seen that DISORT is very close at phase angles from  $15^\circ$  to between  $55^\circ$  and  $110^\circ$ , depending on the illumination angle. The upper value beyond which DISORT either underestimates or overestimates the measured REFF is near the phase angle of  $55^\circ$  for  $\theta_i = 0^\circ$ , the phase angle of  $70^\circ$  for  $\theta_i = 35^\circ$ , and the phase angle of  $110^\circ$  for  $\theta_i = 60^\circ$ . All three approximation models have larger errors than DISORT. Compared with the HIMSA, the improved Hapke model (HAMSA) is a better approximation in the backscattering region but as much as 10% higher than measurements in the region in which DISORT works well. The LB model is always too low in all phase angle ranges, which is caused by the

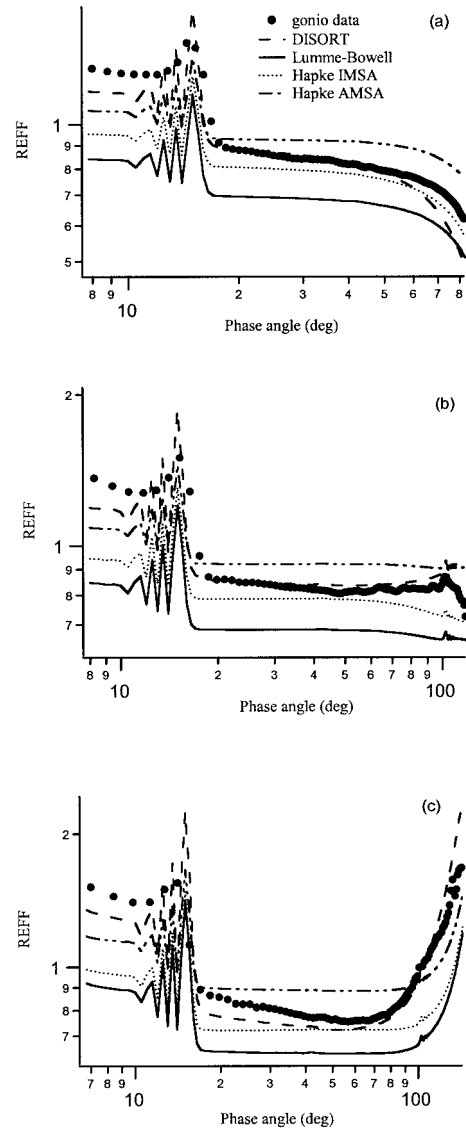


Fig. 5. Comparisons of goniometric measurement, DISORT, LB model, HIMSA, and HAMSA for a 10-mm-thick ( $\tau = 88.5$ ), 200- $\mu\text{m}$ -sphere layer. Incident zenith angles are (a)  $0^\circ$ , (b)  $-35^\circ$ , and (c)  $-60^\circ$ .

similarity-relation-transformed albedo [Eq. (16)] used in the  $H$  function. If instead the original single-scattering albedo is used in the LB model [Eq. (15)], one returns to Eq. (39), which is the same as the Hapke model.

Figure 6 shows comparisons for the 600- $\mu\text{m}$  sphere sample. In this case all models other than the LB model predict much higher values than the measurements. While the LB model appears to make the best prediction, in the 200- $\mu\text{m}$ -sphere case the LB model is shown to have a multiple-scattering part that is too low. The huge difference between the data and DISORT could possibly be attributed to errors from (1) a nonideal condition of the 600- $\mu\text{m}$  spheres, (2) an incorrect estimate of  $\varpi_0$  or  $n_i$ , (3) an insufficient number of spheres in a rela-

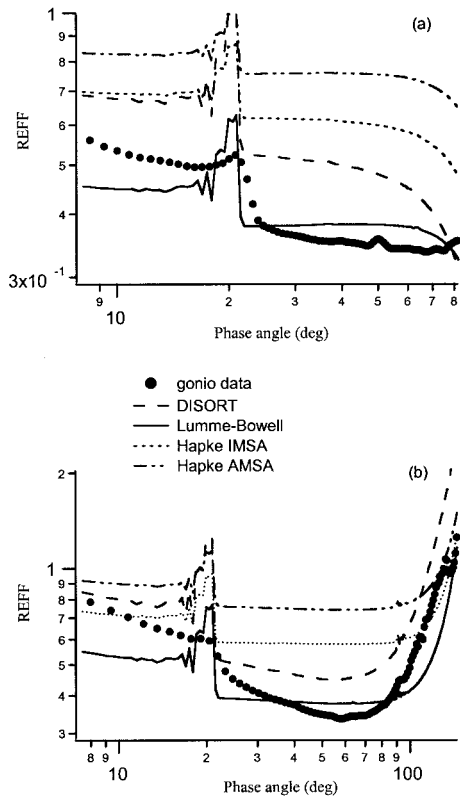


Fig. 6. Comparisons of goniometric measurement, DISORT, LB model, HIMSA, and HAMSAMSA for a 15-mm-thick ( $\tau = 41.25$ ), 600- $\mu\text{m}$ -sphere layer. Incident zenith angles are (a)  $0^\circ$  and (b)  $-60^\circ$ .

tively small sample holder to produce statistically correct RTE results. The first error source is almost certain. Visually, with a  $15\times$  eyepiece, the 600- $\mu\text{m}$  spheres are found to include quite a few nonspherical grains including spheroids, broken spheres, and even some grains that appear colored. This could also be deduced from the data (Fig. 6) where the rainbow feature is small at normal incidence and basically does not exist at  $60^\circ$  incidence, indicating that the 600- $\mu\text{m}$  spheres either contain many nonspherical grains or have greater absorption than estimated. For the second possible error, although in principle one can run the Mie code and then DISORT with various trial combinations of  $n_i$  and  $\omega_0$  to find the best values to fit the data, it is not helpful from the predictive point of view. For the third possibility, although it is argued in Section 3 that our light spot sizes can be regarded as infinite plane-parallel beams, no criterion of how the RTE would work is available at this stage. A filling factor of 0.54 for this sample is well below the lower limit of the typical random close packing value of 0.6 (Ref. 44); thus the sampled scattering volume might not be statistically big enough and local packing structures could affect the scattering patterns. In fact we found in repeated measurements that the 600- $\mu\text{m}$  spheres have larger sample-to-sample variations than the 200- $\mu\text{m}$  spheres. More experimental results are needed to answer these questions.

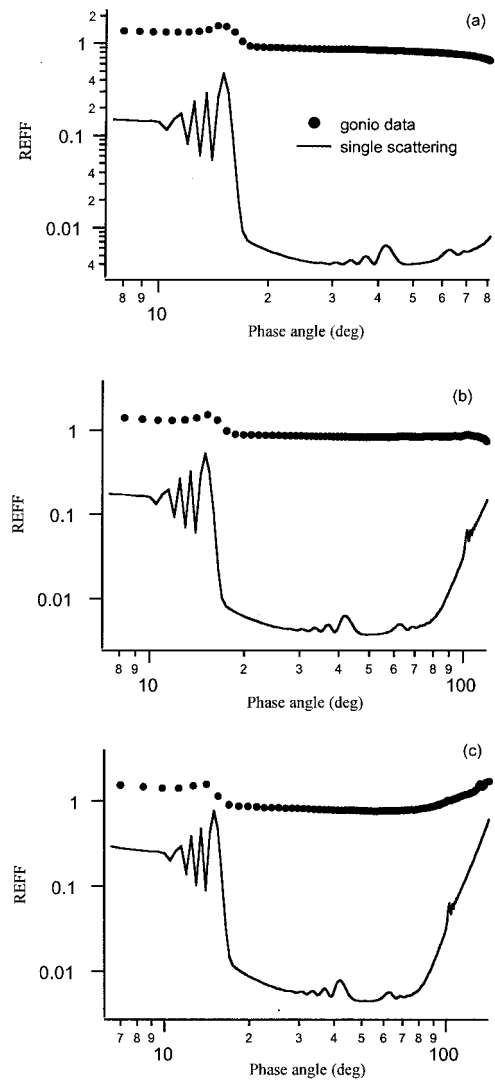


Fig. 7. Contributions of single scattering [Eq. (42)] to total reflectance at (a) normal, (b)  $-35^\circ$ , and (c)  $-60^\circ$  incidence.

## 5. Discussion

### A. Close Packing, Multiple Scattering, and Backscattering

Although there is evidence of many single-scattering features, single scattering contributes only a small fraction to the total scattered power. Figure 7 shows the REFF of the measurement data for the 10-mm-thick layer and the single-scattering approximation predicted by Eq. (42) for the 200- $\mu\text{m}$  spheres at three incident angles. It can be seen that the single-scattering contribution is several tens of percent within the rainbow and drops down to a few percent outside of it. This low fraction remains quite flat until the phase angle of  $100^\circ$  (for  $35^\circ$  and  $60^\circ$  incidences) where it starts to climb to  $\sim 10\%$  and further to nearly 70% around the grazing angle (for  $60^\circ$  incidence). However, the REFF minimum is of the order of 80%. This may semiquantitatively explain why, for the 200- $\mu\text{m}$  spheres, the peaks in the

Mie phase function around the 40° phase angle have been totally washed out while those around 100° (the second-order rainbow) are evident in the REFF. This also shows that since both the rainbow and the grazing regions consist of larger single-scattering contributions they are also more sensitive to surface roughness caused by packing structures.

The reflectance data for both samples (Figs. 5 and 6) show that during the progression from normal to oblique incidence, the forward scattering is never as strong as the backscattering peak until the phase angles are greater than 100°. This demonstrates that intrinsically forward-scattering particles, when in aggregate, can look like backscattering in reflectance measurements<sup>2,4</sup>; thus inverting reflectance data to retrieve single-scattering quantities should be done cautiously. And for complete inversion, reflectance data at larger phase angles are required.

Even for measurements for which the strict RTE has partial success (Fig. 5) the backscattering peaks are ~10% higher than predicted in the smallest phase angle region (~8°). Because of mechanical interference the current goniometer can detect only scattered radiance at phase angles greater than 7°; thus opposition effects that are normally observed in the phase angle range of 2° to 7° are not detected here. This backscattering range is perhaps among the most poorly understood in radiative-transfer theory. Neither semi-empirical model can predict this enhancement. Since LB's shadowing factor [Eq. (21)] is monotonically decreasing from a value of 0.5 at a 0° phase angle, it cannot bring up the REFF values predicted by DISORT. Although Hapke's hot-spot function in Eq. (4) can increase the REFF value's single-scattering part at a 0° phase angle by a factor as great as 2, its  $B_0$  parameter seems hard to predict.

## B. Diffraction

As introduced in Subsection 2.F, both the Hapke and LB models treat diffraction as undistinguishable from the incident flux; thus the diffraction peak should be removed when Mie phase functions are used. To evaluate the accuracy of this assumption, we performed the so-called  $\delta$ - $N$  approximation computations.<sup>26,47</sup> This operation separates the phase function  $P$  into the sum of a  $\delta$  function to replace the forward-scattering peak and a truncated phase function  $P^*$ . Thus Eq. (33) becomes

$$P(\cos \Theta) \approx 2f\delta(1 - \cos \Theta) + (1 - f) \times \sum_{l=0}^{2N-1} (2l + 1)g_l^* P_l(\cos \Theta), \quad (53)$$

where

$$g_l^* = \frac{g_l - f}{1 - f} \quad (l = 0, \dots, 2N - 1), \quad (54)$$

$$f = g_{2N}. \quad (55)$$

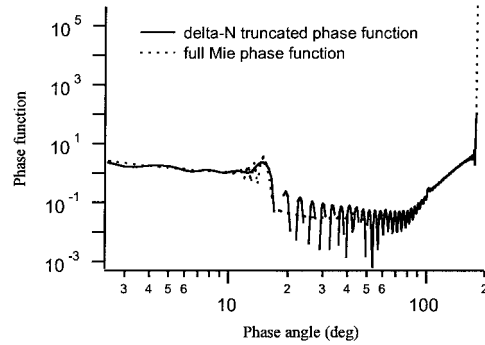


Fig. 8. Comparison of  $\delta$ - $N$  truncated Mie phase function and the full phase function for the 200- $\mu$ m spheres.

Since in this study the DISORT calculations were done with 100 streams (NSTR of 100 in the DISORT code), here we take  $2N = 100$ . In other words we supply DISORT with the input phase functions

$$P^{\text{trunc}}(\cos \Theta) \approx \sum_{l=0}^{99} (2l + 1)(g_l - g_{100})P_l(\cos \Theta) \quad (56)$$

but keep the optical thickness  $\tau$  unchanged. Note that although the DISORT (version 2.0 and later) internally performs the  $\delta$ - $N$  transformation [Eqs. (53)–(55)] to achieve optimum computational efficiency and accuracy for strongly forward-peaked phase functions,<sup>48</sup> it also performs the Nakajima–Tanaka intensity corrections<sup>49</sup> to recover the accurate single and double scatterings. Thus in contrast to supplying DISORT with the full phase function, supplying Eq. (56) has the diffraction peak removed.

Figure 8 shows a comparison of the  $\delta$ - $N$  truncated Mie phase function and the full Mie phase function for the 200- $\mu$ m spheres. The oscillations in the  $\delta$ - $N$  phase function are well known<sup>48,50</sup> and get worse for a smaller  $N$ . Figure 9 shows a comparison of DISORT, a  $\delta$ - $N$  truncated Mie phase function supplied DISORT (DISORT delta- $N$ ), and HAMSA for the 200- $\mu$ m spheres. This example demonstrates the following: (1) The HAMSA is a significant improvement over the HIMSAs in approximating the diffraction-removed numerical RTE solution over a rather large phase angle range (which agrees with DISORT delta- $N$ ). The improvement is very good in the backward direction, and the overall agreement is the best at 35° incidence. (2) Treating diffraction as unscattered may not be a good approximation for this specific example, because HAMSAs (and now DISORT delta- $N$ ) overestimates the REFF through much of the phase angle range for the 200- $\mu$ m spheres. This specific example also shows that the diffraction peak has a significant effect on the multiple-scattering REFF.

Although we have demonstrated with this rather anomalous 200- $\mu$ m-sphere sample (weakly absorbing, highly anisotropic) that the semiempirical models may not work as well as the numerical RTE models from the prediction point of view, this does not have to be true for general situations, especially for

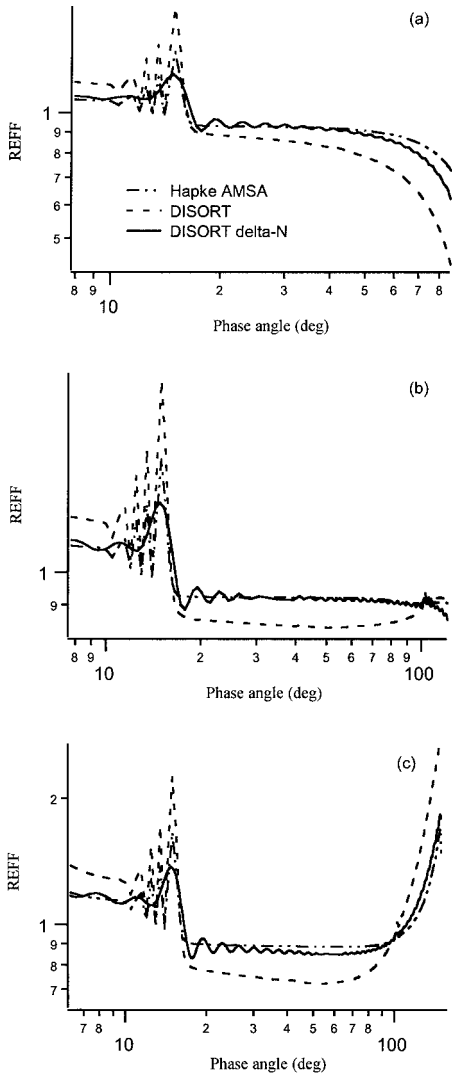


Fig. 9. Comparisons of HAPSA, DISORT, and  $\delta N$ -DISORT for a 10-mm-thick ( $\tau = 88.5$ ), 200- $\mu\text{m}$  layer. Incident zenith angles are (a)  $0^\circ$ , (b)  $-35^\circ$ , and (c)  $-60^\circ$ .

low albedo celestial bodies for which multiple scattering is less anisotropic. Indeed, the widely used Hapke and LB models have found a multitude of applications especially in comparative planetary studies.<sup>23,31,51</sup>

### C. Surface-Roughness Effects

For the 200- $\mu\text{m}$  sample for which the predicted RTE is better the discrepancies between DISORT and the measurements in the forward-scattering region could be attributed to surface roughness because measurements in this region have the largest sample-to-sample variations. There are two competing theories<sup>7,9,52</sup> of the surface roughness of packed surfaces, and both decrease the REFF at larger viewing angles. In this study the LB theory is chosen because the case for the packed-sphere surface [Eq. (18)] is well documented. Since all the measurements here are on macroscopically flat surfaces, the term rough-

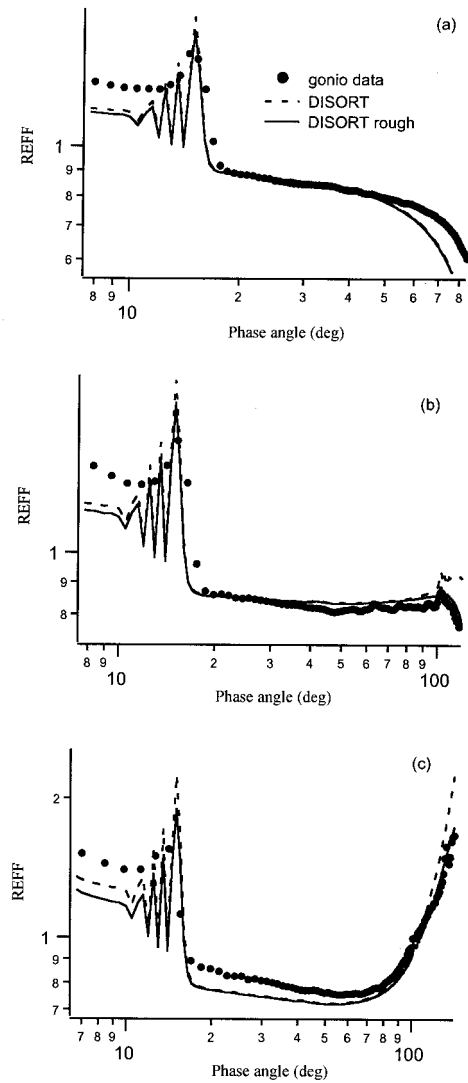


Fig. 10. Comparisons of DISORT, roughness-corrected DISORT, and the measurements. Incident zenith angles are (a)  $0^\circ$ , (b)  $-35^\circ$ , and (c)  $-60^\circ$ .

ness refers only to microscopic roughness with scales of several particle diameters but not as large as sastruga on snow.<sup>53</sup> The Hapke roughness model, which appears to be more appropriate for large-scale roughness, consists of an average tilting angle  $\bar{\theta}$  [in Eq. (4)] of the local facet; thus it is hard to predict for packed spheres. Although it is argued in Subsection 2.F that applying the LB roughness factor to the whole RTE model may be physically plausible, the discussions in Subsection 5.A show that single scattering contributes a significant amount in the forward direction; thus the LB roughness correction is applied to the single-scattering term only.<sup>29</sup> Specifically the roughness-corrected DISORT is

$$\text{DISORT}^{\text{Rough}} = \text{DISORT} - (1 - \Phi_R) \frac{\omega_0}{4} \frac{1}{\mu + \mu_0} P(\alpha), \quad (57)$$

where  $\Phi_R$  is given in Eq. (18). In this work the filling factor of 0.60 leads to a  $\rho$  value of 1.1 for the 200- $\mu\text{m}$ -sphere sample. The parameter  $q$ , the fraction of a surface covered with holes, is specified as 1 as implied by the discussions on the packed surface of spheres in Ref. 9. Figure 10 shows comparisons of the measurements of DISORT and LB roughness-corrected DISORT. At normal incidence [Fig. 10(a)] the correction has little effect. For 35° and 60° incidences, although this correction factor further reduces the DISORT values in the backscattering direction, it improves the agreement in the grazing angles. Since single scattering contributes tens of percentage points in these two regions, applying the roughness correction to single scattering changes the intensities significantly. Again a predictive enhanced backscattering theory is needed to describe accurately the hot spot in the measurements.

## 6. Conclusions

We have performed controlled laboratory BRDF measurements on NIST-traceable nearly monodisperse sphere samples and compared these measurements with five radiative-transfer models. It has been found that the numerical solution of the RTE (DISORT and MBRF) can predict the BRDF well over a large phase angle range, especially at oblique incidence for the 200- $\mu\text{m}$ -diameter polymer spheres. Semiempirical models such as the Hapke and Lumme–Bowell models predict less anisotropic scattering than the strict RTE and the measurements. From the prediction point of view, numerical RTE models such as DISORT or MBRF work much better than semiempirical models for nearly monodisperse spherical particles. Use of the scaled single-scattering albedo in the multiple-scattering term in the Lumme–Bowell model can seriously underestimate the total scattered radiance. When Lumme–Bowell’s surface-roughness correction is combined with a numerical RTE, the REFF at oblique incidence can be predicted very well except in the backscattering direction.

Significant single-scattering features are retained even when the spheres are closely packed with filling factor values higher than 0.5. However, the overwhelming multiple scattering tends to wash out some of the sharp features present in single scattering.

The current study suggests that more extensive reflectance measurements on samples with known single-scattering properties are desired to test further the current scattering models. More RTE modeling efforts, especially applicable to high-density media, can also be appropriate. It is also anticipated that diffraction effects must be considered in order to model the particle scattering more accurately.

This study was supported by the Ocean Optics program at the Office of Naval Research. We thank Howard Gordon for discussions during this study, Al Chapin for help constructing the goniometric scattering meter, and Michael Mishchenko for communication on his BRDF model. The constructive comments

from two anonymous reviewers have significantly improved the quality of this paper.

## References

1. B. Hapke and E. Wells, “Bidirectional reflectance spectroscopy 2. Experiments and observations,” *J. Geophys. Res.* **86**, 3055–3060 (1981).
2. M. I. Mishchenko, “Asymmetry parameters of the phase function for densely packed scattering grains,” *J. Quant. Spectrosc. Radiat. Transfer* **52**, 95–110 (1994).
3. B. Hapke, “Are planetary regolith particles backscattering? Response to a paper by M. Mishchenko,” *J. Quant. Spectrosc. Radiat. Transfer* **55**, 837–848 (1996).
4. M. I. Mishchenko and A. Macke, “Asymmetry parameters of the phase function for isolated and densely packed spherical particles with multiple internal inclusions in the geometric optics limit,” *J. Quant. Spectrosc. Radiat. Transfer* **57**, 767–794 (1997).
5. B. Hapke, “Scattering and diffraction by particles in planetary regoliths,” *J. Quant. Spectrosc. Radiat. Transfer* **61**, 565–581 (1999).
6. B. Hapke, “Bidirectional reflectance spectroscopy 1. Theory,” *J. Geophys. Res.* **86**, 3039–3054 (1981).
7. B. Hapke, *Theory of Reflectance and Emittance Spectroscopy* (Cambridge University, New York, 1993).
8. B. Hapke, “Bidirectional reflectance spectroscopy 5. Coherent backscatter opposition effect and anisotropic scattering,” *Icarus* **157**, 523–534 (2002).
9. K. Lumme and E. Bowell, “Radiative transfer in the surfaces of atmosphereless bodies. I. Theory,” *Astron. J.* **86**, 1694–1704 (1981).
10. K. Stamnes, S. C. Tsay, W. Wiscombe, and K. Jayaweera, “Numerically stable algorithm for discrete-ordinate-method radiative transfer in multiple scattering and emitting layered media,” *Appl. Opt.* **27**, 2502–2509 (1988).
11. M. I. Mishchenko, J. M. Dlugach, E. G. Yanovitskij, and N. T. Zakharova, “Bidirectional reflectance of flat, optically thick particulate layers: an efficient radiative transfer solution and applications to snow and soil surfaces,” *J. Quant. Spectrosc. Radiat. Transfer* **63**, 409–432 (1999).
12. A. F. Cheng and D. L. Domingue, “Radiative transfer models for light scattering from planetary surfaces,” *J. Geophys. Res.* **105**, 9477–9482 (2000).
13. Y. Shkuratov, A. Ovcharenko, E. Zubko, O. Miloslavskaya, K. Muinonen, J. Piironen, R. Nelson, W. Smythe, V. Rosenbush, and P. Helfenstein, “The opposition effect and negative polarization of structural analogs for planetary regoliths,” *Icarus* **159**, 396–416 (2002).
14. S. Kaasalainen, “Laboratory photometry of planetary regolith analogs. I. Effects of grain and packing properties on opposition effect,” *Astron. Astrophys.* **409**, 765–769 (2003).
15. C. Leroux, J. Lenoble, G. Brogniez, J. W. Hovenier, and J. F. de Haan, “A model for the bidirectional polarized reflectance of snow,” *J. Quant. Spectrosc. Radiat. Transfer* **61**, 273–285 (1997).
16. H. C. van de Hulst, *Light Scattering by Small Particles* (Dover, New York, 1957).
17. C. F. Bohren and D. R. Huffman, *Absorption and Scattering of Light by Small Particles* (Wiley, New York, 1998).
18. A. A. Kokhanovsky and E. P. Zege, “Scattering optics of snow,” *Appl. Opt.* **43**, 1589–1602 (2004).
19. S. Chandrasekhar, *Radiative Transfer* (Dover, New York, 1960).
20. M. I. Mishchenko, “Diffuse and coherent backscattering by discrete random media. 1. Radar reflectivity, polarization ratios, and enhancement factors for a half-space of polydisperse,

- nonabsorbing, and absorbing spherical particles," *J. Quant. Spectrosc. Radiat. Transfer* **56**, 673–702 (1996).
21. M. I. Mishchenko, "The angular width of the coherent backscatter opposition effect—an application to icy outer planet satellites," *Astrophys. Space Sci.* **194**, 327–333 (1992).
  22. K. Lumme and W. M. Irvine, "Radiative transfer in the surfaces of atmosphereless bodies. III. Interpretation of lunar photometry," *Astron. J.* **87**, 1076–1082 (1982).
  23. E. Bowell, B. Hapke, K. Lumme, J. Peltoniemi, and A. W. Harris, "Application of photometric models to asteroids," in *Asteroids II*, R. P. Binzel, T. Gehrels, and M. S. Matthews, eds. (University of Arizona, Tucson, Ariz., 1989), pp. 524–556.
  24. J. I. Peltoniemi and K. Lumme, "Light scattering by closely packed particulate media," *J. Opt. Soc. Am. A* **9**, 1320–1326 (1992).
  25. E. G. Yanovitskij, *Light Scattering in Inhomogeneous Atmospheres* (Springer-Verlag, Berlin, 1997).
  26. G. E. Thomas and K. Stamnes, *Radiative Transfer in the Atmosphere and Ocean* (Cambridge University, New York, 2002).
  27. J. K. Hillier, "Shadow-hiding opposition surge for a two-layer surface," *Icarus* **128**, 15–27 (1997).
  28. B. Hapke, "The Lumme–Bowell photometric parameters—reality or fantasy?" *Bull. Am. Astron. Soc.* **14**, 726H (1982).
  29. K. Lumme and E. Bowell, "A reply to Hapke's criticism of the Lumme–Bowell photometric theory," *Bull. Am. Astron. Soc.* **14**, 726H (1982).
  30. A. A. Kokhanovsky, "On light scattering in random media with large densely packed particles," *J. Geophys. Res.* **103**, 6089–6096 (1998).
  31. B. Hartman and D. Domingue, "Scattering of light by individual particles and the implications for models of planetary surfaces," *Icarus* **131**, 421–448 (1998).
  32. C. Bruegge, N. Chrien, and D. Haner, "Spectralon BRF data for MISR calibration applications," *Remote Sens. Environ.* **76**, 354–366 (2001).
  33. W. C. Tsai and R. J. Pogorzelski, "Eigenfunction solution of the scattering of beam radiation fields by spherical objects," *J. Opt. Soc. Am.* **65**, 1457–1463 (1975).
  34. H. Zhang, K. J. Voss, R. P. Reid, and E. M. Louchard, "Bidirectional reflectance measurements of sediments in the vicinity of Lee Stocking Island, Bahamas," *Limnol. Oceanogr.* **48** (1, Part 2), 380–389 (2003).
  35. H. Zhang, K. J. Voss, and R. P. Reid, "Determining the influential depth of sediment particles by BRDF measurements," *Opt. Express* **11**, 2654–2665 (2003), <http://www.opticsexpress.org>.
  36. K. J. Voss, A. L. Chapin, M. Monti, and H. Zhang, "Instrument to measure the bidirectional reflectance distribution function of surfaces," *Appl. Opt.* **39**, 6197–6206 (2000).
  37. A. A. de Rooij and C. C. A. H. van der Stap, "Expansion of Mie scattering matrices in generalized spherical functions," *Astron. Astrophys.* **131**, 237–248 (1984).
  38. M. I. Mishchenko, L. D. Travis, and A. A. Lacis, *Scattering, Absorption, and Emissions by Small Particles* (Cambridge University, New York, 2002).
  39. W. Wiscombe, "Improved Mie scattering algorithms," *Appl. Opt.* **19**, 1505–1509 (1980).
  40. W. J. Wiscombe, "Mie scattering calculations: Advances in technique and fast, vector-speed computer codes," NCAR Tech. Note (National Center for Atmospheric Research, July 1979, revised Aug. 1996), [ftp://climate.gsfc.nasa.gov/pub/wiscombe/Single\\_scatt/](ftp://climate.gsfc.nasa.gov/pub/wiscombe/Single_scatt/).
  41. J. E. Hansen and L. D. Travis, "Light scattering in planetary atmospheres," *Space Sci. Rev.* **16**, 527–610 (1974).
  42. C. F. Bohren, "Multiple scattering and some of its observable consequences," *Am. J. Phys.* **55**, 524–533 (1987).
  43. S. Liang, "An investigation of remotely sensed soil depth in the optical region," *Int. J. Remote Sens.* **18**, 3395–3408 (1997).
  44. G. D. Scott, "Packing of Spheres," *Nature (London)* **188**, 908–909 (1960).
  45. X. Ma, J. Lu, R. S. Brock, K. M. Jacobs, P. Yang, and X. Hu, "Determination of complex refractive index of polystyrene microspheres from 370 to 1610 nm," *Phys. Med. Biol.* **48**, 4165–4172 (2003).
  46. J. A. Adam, "The mathematical physics of rainbows and glories," *Phys. Rep.* **356**, 229–365 (2002).
  47. W. J. Wiscombe, "The delta-M method: rapid yet accurate radiative flux calculations for strongly asymmetric phase functions," *J. Atmos. Sci.* **34**, 1408–1422 (1977).
  48. K. Stamnes, S. C. Tsay, W. Wiscombe, and I. Laszlo, "DISORT, a general-purpose Fortran program for discrete-ordinate-method radiative transfer in scattering and emitting layered media: documentation of methodology," Version 1.1, March 2000, [ftp://climate.gsfc.nasa.gov/pub/wiscombe/Multiple\\_scatt/](ftp://climate.gsfc.nasa.gov/pub/wiscombe/Multiple_scatt/).
  49. T. Nakajima and M. Tanaka, "Algorithms for radiative intensity calculations in moderately thick atmospheres using a truncation approximation," *J. Quant. Spectrosc. Radiat. Transfer* **40**, 51–69 (1988).
  50. C. D. Mobley, *Light and Water: Radiative Transfer in Natural Waters* (Academic, New York, 1994).
  51. D. Domingue and A. Verbiscer, "Reanalysis of the solar phase curves of the icy Galilean satellites," *Icarus* **128**, 49–74 (1997).
  52. B. Hapke, "Bidirectional reflectance spectroscopy 3. Correction for macroscopic roughness," *Icarus* **59**, 41–59 (1984).
  53. S. G. Warren, R. E. Brandt, and P. O. Hinton, "Effect of surface roughness on bidirectional reflectance of Antarctic snow," *J. Geophys. Res.* **103**, 25,789–25,807 (1998).